

Build a Ruler to Measure Electron Localization Function with Machine Learning Models: S-Au bonds Quantification in Thiolate Protected Gold Nanoclusters

Xinxu Zhang^{1,5}, Hui Jia^{1,5}, Fangzhen Tian², Yandi Liu³, Ullrich Carsten⁴, Yulong Wu¹, Changlong Liu¹, Xiaodong Zhang^{1,2}, Yonghui Li^{1*}

1. Department of Physics and Tianjin Key Laboratory of Low Dimensional Materials Physics and Preparing Technology, School of Sciences, Tianjin University, Tianjin 300350, China
2. Tianjin Key Laboratory of Brain Science and Neural Engineering, Academy of Medical Engineering and Translational Medicine, Tianjin University, Tianjin 300072, China
3. School of Finance, Tianjin University of Finance and Economics, 25 Zhujiang Rd., Hexi Dist., Tianjin, China. 300222
4. Department of Physics and Astronomy, University of Missouri, Columbia, Missouri 65211, USA
5. These authors contributed equally: Xinxu Zhang, Hui Jia

* yonghui.li@tju.edu.cn

Abstract

Complicated S-Au interaction patterns in thiolate-protected gold nanoclusters (TP-AuNCs) are important in the formation of versatility among clusters. In this study, the ELFnet, a novel convolutional neural network (CNN) model is trained and tested to bridge the electron localization function (ELF) images and the bond lengths. As believed to be a successful bond describer, a dataset of 3959 ELF images is obtained out of Density Functional Theory (DFT) simulations, followed by a series of model architecture and hyperparameter exploration. The ELFnet with its best performance shows its correct feature extraction ability to gain insights in the prediction of bond lengths. Besides, the ELFnet also possess 3 different "ELF reading modes" which inspires other possibilities in understanding ELF images. The ELFnet serves as an "ELF-ruler" to give precise bond type labels (or the predicted bond lengths). Such ELF-ruler measured bond types represent a particular bond when distorted by external factors with a quantitative indicator. With the help of such an ELF-ruler, the classification of chemical bonds in general may be extended to more precise types.

I. Introduction

As the development of first principal calculations, the definition of chemical bonds was once challenged until the introduction of Electron Localization Function (ELF) ^{1,2}. Algorithms such as ELF connect the probabilities in quantum worlds to human-interpretable concepts in practice ³. Bond types such as covalent and ionic are visually distinguishable based on the ELF plots. With dynamics and excited states, ELF has been extended as a time-resolvable way to represent bond transitions in the presents of external fields ^{4,5}. As an indicator of strongly localized electrons, the precision of ELF is affected by the choice of exchange-correlation functional when using as a post-process algorithm after Density Functional Theory (DFT) simulations ⁶. But it is still preferred by its conceptual abstract and being used in various fields ⁷⁻¹¹. Although ELF has a nice probabilistic interpretation (a well-defined domain of value), the interpretation of ELF is still limited by its graphical display with fully-filled details. As it comes to the analysis of nanoclusters (NCs), the rich details in ELF become a disadvantage instead.

Thiolate-protected gold NCs (TP-AuNCs) draw so much attention in the past decade for their special structures, quantum properties, customizability, wide applications and great potential ¹². After the unveiling of the two structures of TP-AuNCs back in 2007 ¹³ and 2008 ¹⁴, the investigations of their electron structures become more and more important. At the atomic level, the S-Au interactions are as critical as gold-gold interactions in TP-AuNCs ¹⁵. S-Au interaction is related to the

balance between core-ligands binding and core cohesivity^{16,17}. As the S-Au interactions being investigated with relatively brief indicators such as binding energy¹⁸, ELF based analysis should give it a better resolution.

Back to the field of TP-AuNCs design and investigation, an interesting probability-based algorithm has been proposed¹⁹. S-Au bonds are described by their local environments and such a way of description appears to be a nice approach. Inspired by such work, we propose a new way of the investigation of the S-Au interactions by a detailed analysis of their local electron structures based on ELF analysis. Considering the great success, it is well-acknowledged that the bonding details are captured by ELF. Therefore, to complete the puzzle of ELF interpretation, a detail-oriented algorithm is very important. So, in this work, we focus on the S-Au interaction TP-AuNCs and introduce an ELF interpretation algorithm.

II. Experimental facts, the dataset and the algorithm

a. Experimental evidence of the S-Au interaction

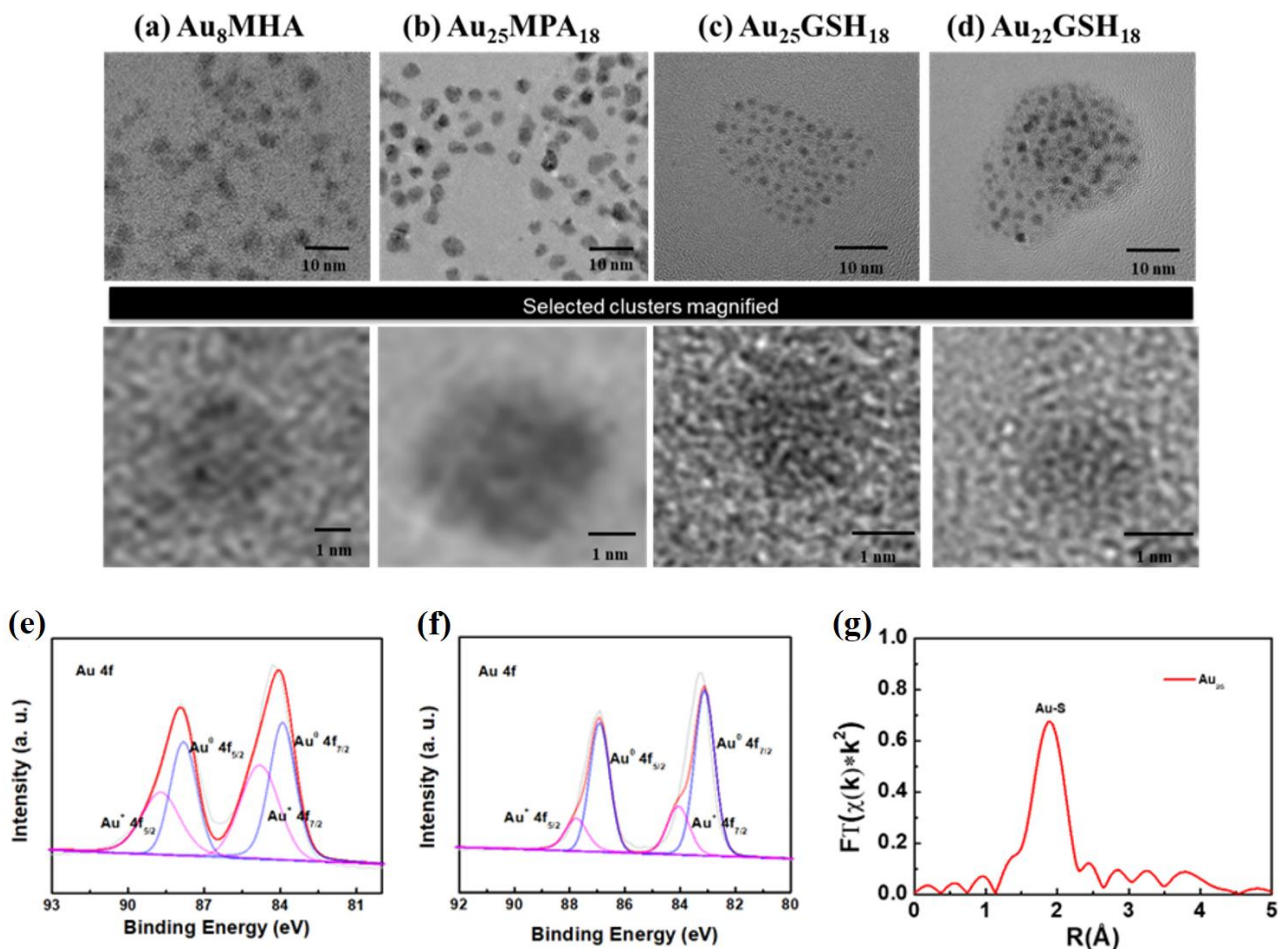


Figure 1 TEM images of 4 synthesized clusters. XANES data to show S-Au bonds

To validate the S-Au interaction shifts among clusters, some experimental tests are made based on synthesized clusters. Figure 1a-d shows the TEM images of 4 types of clusters.

The Figure 1e-g is the XANES to show bonding status between S-Au. Bonds vary across different clusters. As shown in Fig e, f, the two doublet 4f peaks in the high-resolution spectrum of Au 4f suggest that there are two different elemental chemical states of Au species. The Au 4f_{5/2} and Au 4f_{7/2} peaks with binding energies of 87.8 and 83.9 (Figure 1e), 86.9 and 83.1 eV (Figure 1f) are ascribed to metallic Au (Au⁰), and the other doublet at 88.7 and 84.7 (Figure 1e), 87.75 and 84.05 eV for Au 4f_{5/2} and Au 4f_{7/2} are assigned to Au⁺ ion. The Au⁰ belongs to the S-Au bond, whose content determined by XPS. The result showed that the content of S-Au in Au₂₅MPA₁₈ is less than it in Au₂₅GSH₁₈. Also, the

lower binding energy of Au^+ in MPA indicates a lower oxidation state, implying it easier to lose electrons, and the more unstable S-Au bond. Furthermore, the S-Au bond length of S-Au in the $Au_{25}MPA_{18}$ is 2.3 Å (Figure 1f), and in $Au_{10}(SR)_{10}$ is 2.31 Å. To summarize, gold clusters with different ligands or number of gold are corresponding to different binding energies and different bond lengths of S-Au. Thus, a detailed algorithm must be designed.

b. The dataset of ELF images

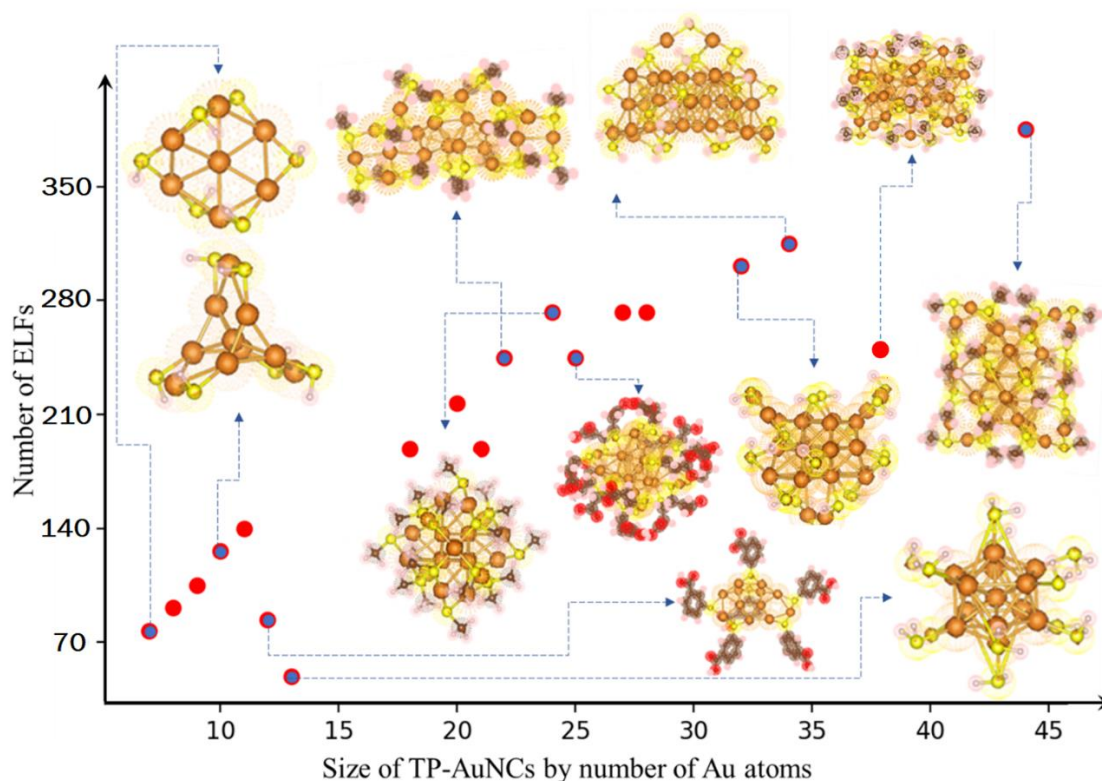


Figure 2 TP-AuNCs in the literature collected and presented in a coordinate space of number of Au atoms and number of ELF images.

The dataset contains 25 TP-AuNC structures collected from previous work (see Table S1) and all of them are verified by XRD results or DFT simulations. Based on structures, DFT single point simulations are performed with B3LYP exchange-correlation potential. To better describe the S-Au interaction, the basis sets of sulfur and gold are 6-311++G(3df,3pd) and cc-pVDZ-pp²⁰. DFT simulation results are obtained by using Gaussian 09²¹ and post-process are performed with Multiwfn²².

ELFs are believed to be good descriptors of chemical bonds. The Definition of the ELF¹ is based on the comparison between the kinetic energy density in a particular system, $D_{\sigma}(\vec{r})$ and in the uniform electron gas $D_{\sigma}^0(\vec{r})$:

$$ELF(\vec{r}) = \frac{1}{1 + \left[\frac{D_{\sigma}(\vec{r})}{D_{\sigma}^0(\vec{r})} \right]^2}. \quad (1)$$

Such comparison allows people to identify the locality of electrons in the system. The value of ELF has a nice probability explanation which ranges from 0 to 1. In many publications, ELF=0.8 is selected to be the threshold²³⁻²⁵ to demonstrate bonds where the single, double and triple covalent bonds can be visualized easily. When ELF=0.5, the electrons behave like free electrons. But as we shall demonstrate in the next section, information contained in ELF is way beyond some simple thresholds.

Based on the electron densities and Kohn-Sham orbitals simulated, ELF images can be generated. We first select two neighboring sulfur and gold (distance < 2.7 Å) and build a square with the S-Au bond located at the center of the square and side lengths of the square equals to the S-Au bond. The normal direction of the square can be selected randomly. Then the ELF values on the square is considered an ELF image and collected into our dataset. Due to the limitation of known TP-AuNC structures, data augmentation is applied by taking ELF images along 7 different directions (directions are

defined by the normal directions of planes of the sulfur, the gold and an extra neighboring atom). Such augmentation extends 662 S-Au bonds to 4527 (the augmentation fails on some NCs. See Table S1 for more details). The images are then filtered for some poorly behaved images due to the inappropriate selection of the square or software failure. The filtered dataset contains 3959 ELF images. In addition, since the ELF does not distribute evenly across various bond lengths, the ELFs corresponds to larger bond lengths are duplicated to improve the prediction accuracy in the region of long bond length side. Concretely, bonds range in [2.3 Å, 2.4 Å], [2.4 Å, 2.5 Å], [2.5 Å, 2.6 Å], and [2.6 Å, 2.7 Å] receive weights of 1, 2, 20 and 30 (examples are shown in Figure S2). Weights are added directly to the model by duplication. As a result, the final dataset contains 8061 200×200 ELF images. The obtained dataset keeps all ELFs generated with the same foundation, thus allows the pattern recognition algorithm works.

c. Identify bond lengths by ELF images

As we believed, ELF images are rich in details of bond information. Therefore, an ELF image is sensitive to bond lengths. With such consideration, a hypothesis can be raised: given an ELF image, a sharp observer should be able to identify the associated bond length. Such task is difficult for human observers but it may be suitable for a convolutional neural network (CNN). The strategy of training an “AI ELF expert” is shown in Figure 3. Once such CNN model is successfully trained, it can be used as an “ELF-ruler”.

Since the ELF function is well defined in its range, the standardization of ELF images uses 0.5 and 0.5 as the values of average and standard deviation (models with batchnorm is explained in the next section). The dataset is split into a training set and a cross-validation set with a ratio of 7:3. All the images are tagged with the associated bond lengths. MSE loss and Adam are used as loss function and optimizer.

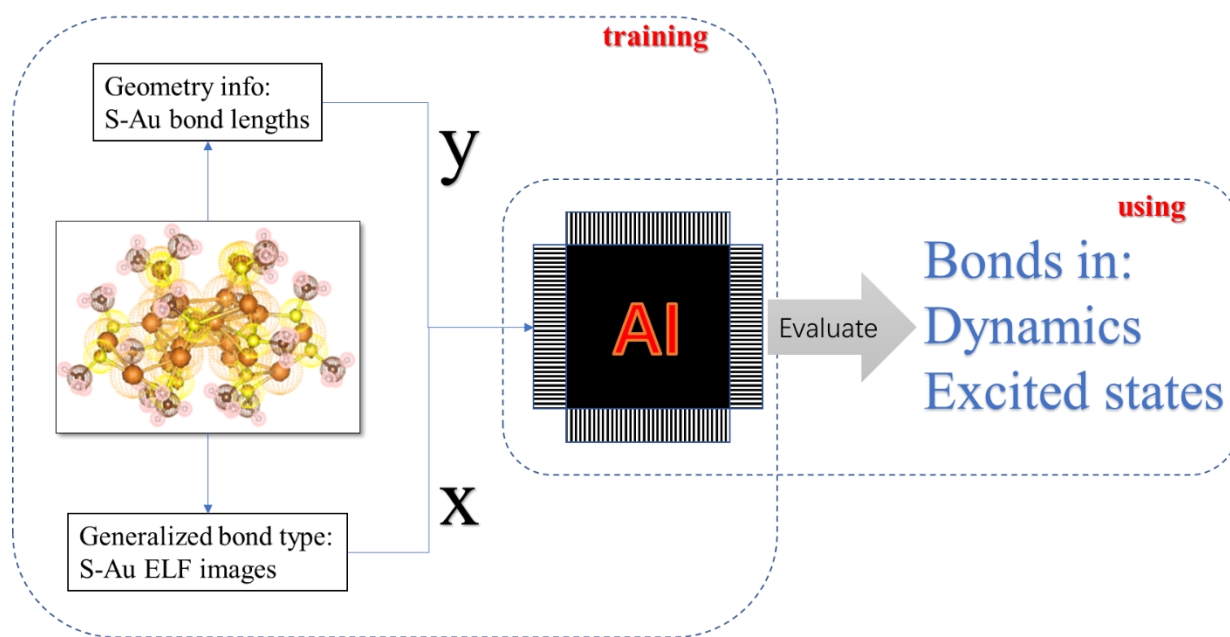


Figure 3 Strategy of building an ELF based AI algorithm for the bond evaluation purpose.

III. Results and discussion

a. Model exploration and the Best CNN model

The ELF dataset allows us to construct and improve a CNN model iteratively. Tens of CNN models are testified during the improvement of the CNN model. The tested models vary among network depth, size of the convolution kernels, number of CNN extracted features and choices of regularization layers. These are the major considerations to reduce overfitting as well as improve prediction precision.

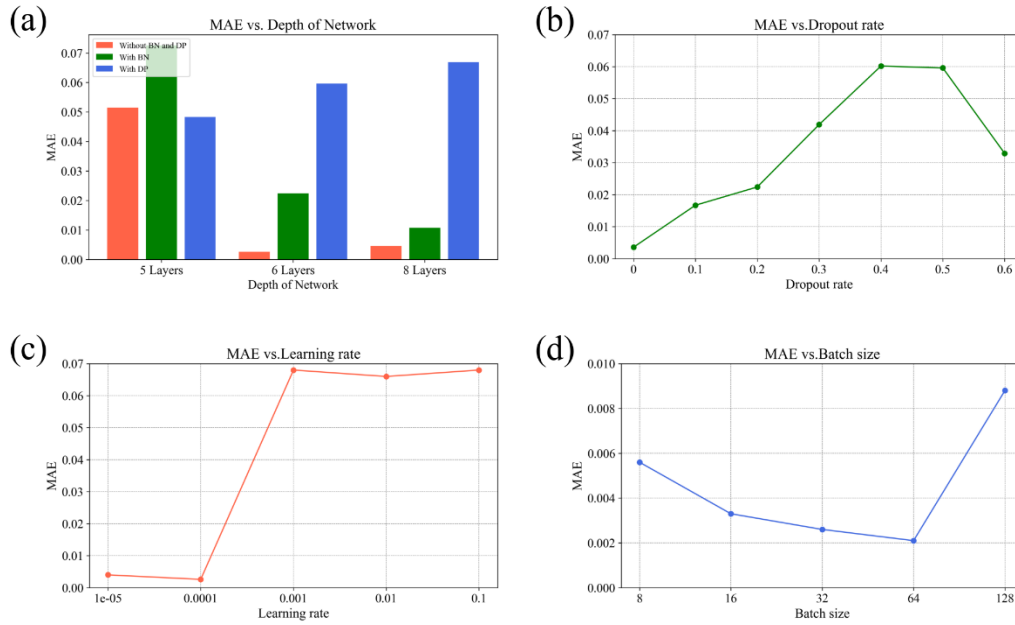


Figure 4 Errors of cross-validation set in CNN design and training: a) Errors in CNN design with or without batchnorm and dropout layers in 5-, 6- and 8-layer CNN models. b) Errors in CNN models with dropout layers and different dropout rates. Errors of a typical CNN model trained with different c) learning rates and d) batch sizes.

Constrained by the scale of our dataset and inspired by GoogleNet, the regularization layers including batch normalization (BN) layers and Dropout (DP) layers are implemented and tested in the initial draft of our CNN model. Since BN layers can normalized extracted features, it is believed to stabilized the training procedures. DP layers drop out a portion of neurons randomly in the forward-propagation stage, and yield a more robust CNN propagation structure. However, as shown in Figure 4a, models with BN or DP layers perform poorer than the CNN model without regularization layers. The failure of BN layers indicates that the ELF images need no further normalization since the ELF function is based on a physical oriented probabilistic explanation. Any transformation (applying a same scaling or shift to all images is excluded) may break the physical orientation and make the comparison of transformed images invalid. The failure of DP layers indicate that ELF images are dense in the concentration of information. Thus, the extracted features should not be ignored to match the continuous nature of their tag. This can also be proofed by Figure 4b, when the dropout probability is not zero, the MAE is always significantly larger. As indicated by the linear correspondence between the Mean Absolute Error (MAE) and the dropout rate (when the dropout rate below 0.5), the more features dropped, the more error can be seen in the predictions.

Based on the previous iteration, models with different layers are implemented and tested. Models with 6 layers performs well among all models. 6 layers seem to be the best number with a good feature extraction capability under the data limitation of current dataset. It is generally acknowledged that the higher the resolution of the images is, the deeper the net can be designed. The resolution, which is calculated by formulas, can be enhanced to any resolution, but it is difficult for our dataset to support a deeper model. A layer in the context refers specifically to a convolutional layer in the model. There are additional layers such as activation functions and pooling layers for further processing of the features extracted by the convolutional layers in general, but the number and types of following layers are not included in the description of layers explicitly.

With important concern that the regularization layers should not be implemented and the best number of layers should be 6, the model is trained with different learning rates and batch sizes (Figure 4c-d). The learning rate cannot set beyond 1×10^{-4} to prevent the potential failure in the “saddle points” of the super parameter space. Besides, the batch size must be set to 64 to achieve the lowest MAE. Last, both applications of activation layers and pooling layers are tested. Using the Rectified Linear Unit (ReLU) as activation layers performs slightly better than using LeakyReLU, an activation algorithm that allows scaled negative values. Besides, max pooling layers perform better than average pooling layers.

b. The best performed CNN model: the ELFnet

Based on the iterations of improvement described above, the best performed CNN model, the ELFnet is shown in Figure 5a. The ELFnet reads ELF images and predict the associated bond lengths. It contains 6 convolutional layers followed by 6 ReLU activation layers and 5 max pooling layers. There are 256 features flattened after the extractions of convolutional layers. Then, the features are feed to two consecutive fully connected layers and return a final output.

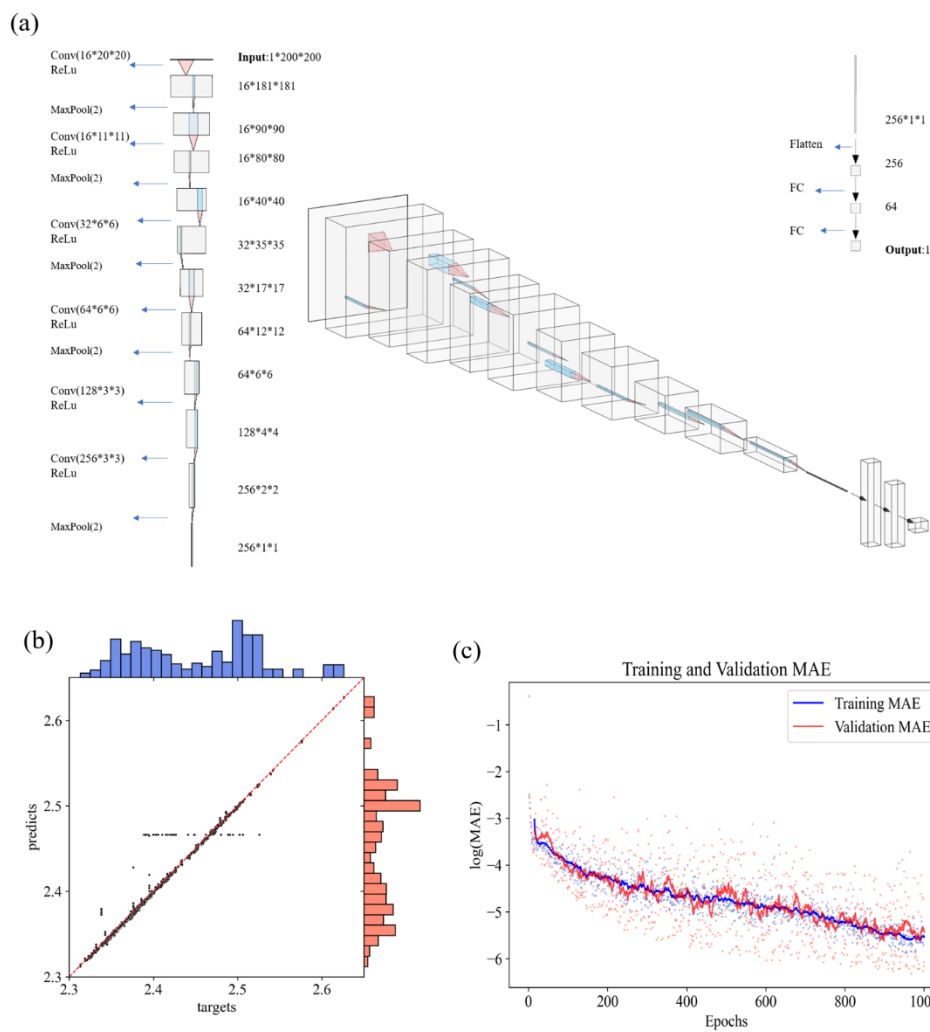


Figure 5 a) The network structure with details of the ELFnet, the model with best performance based on our ELF dataset. b) the prediction-tag comparison. Most result lies on the straight line which indicates the high precision of the model prediction. The distributions of labels and predictions are shown in the joint plots. c) the logarithm of MAE as a function of epochs in training. At epochs 900-1000, the MAEs in training and validation begin to diverge. The dots are the actual data, the solid lines are the moving average of the actual data points.

To evaluate the ELFnet, the joint plot of the prediction-tag curve and the data distribution provided in the joint plots is presented in Figure 5b. After a 5-fold cross-validation, ELFnet predicts the bond length with a small Mean Absolute Error (MAE) of about 0.0021 Å, approximately 0.1% of a typical S-Au bond length. The predicted distribution and the actual distribution of tags are very close, indicating that there is no bias in the predictions. Additionally, there are a few incorrect prediction points, but their share is as small as 0.5% in the full dataset. Even with these incorrect predictions, the performance of ELFnet is still adequate in practice. The training procedure is shown in Figure 5c. As the training and cross-validation errors begin to diverge around 900-1000 epochs, the training is stopped.

c. What does the ELFnet see in predicting bond lengths?

The ELFnet does not require any predefined value for ELF such as 0.8 or 0.5. Therefore, it analyzes ELF images in a different way than the way of human. To obtain outputs of convolutional layers, a forward hook function after each convolutional layer is implemented in the model. For each convolutional layer, extracted features are summed up to obtain a total feature map. And typical visualizations of extracted features of each convolutional layer are shown in Figure 6. The first convolutional layer sharpens the edges and makes the boundary between the low value zones and the high value

zones. The second convolutional layer makes the edge even sharper. The edges and critical positions are clearly shown in the third convolutional layer: the ELFnet focuses on the two bands (between the 3 dark stripes in the middle of the image) and there are some features on the gold side as well. As the network progresses, the feature map size gradually becomes smaller and the extracted features are compacted without a human readable form. The third convolutional layer shows a machine way of reading ELF image: the zone between atoms is very important and features should be extracted. Besides, there could be some features located on the gold atom side which can be linked to the distortion of other valence electrons. Such machine aided ELF reading considers more than human reading.

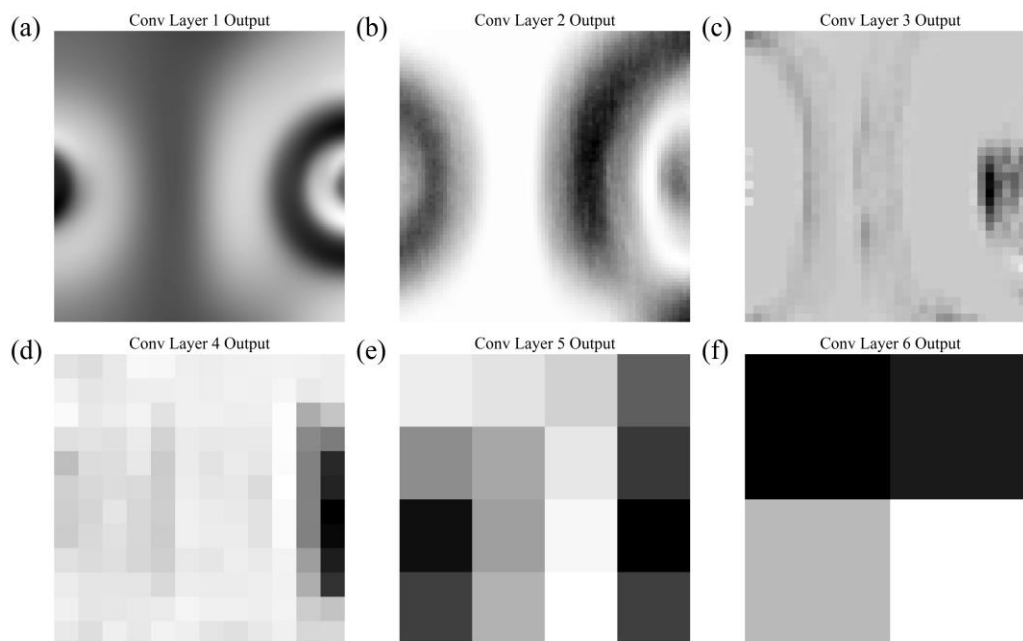


Figure 6 image plots of summations of features extracted from different convolutional layer

To better understand the decision process of the neural network, Gradient-weighted Class Activation Mapping (Grad-CAM) algorithm has been applied to the last convolutional layer of the ELFnet. Grad-CAM plots allow more in-depth explanation of the model's decision process. As shown in Figure 7, the ELFnet feature extraction process varies among ELF images, although the ELF images appear similar to human. 6 frequently seen variances of feature extractions are selected. Since the features are plotted by the rainbow color scheme, the ELFnet will focus more on areas of red than areas of blue.

There are 3 patterns that can be seen from Grad-CAM plots. As shown in Figure 7a, c, and f, the ELFnet mainly scans from the gold atom side to the central region to determine the S-Au bond length. In such a mode, ELFnet extracts information similar to the way of human (e.g., reading covalent bonds) but with more details. This mode should be called the “regular mode I”. But depending on other impacts on the gold side ELF, the ELFnet may focus more on a particular region instead of reading the gold side indiscriminately. The ELFnet may focus on the sulfur side in some cases rather than the gold side (Figure 7d). Such pattern should be called “regular mode II”, it is very similar to the “regular mode I” but scans in the opposite direction. The frequency of seeing the “regular mode I” is more than the “regular mode II” and such frequency difference indicates that the gold is more important in the S-Au bond. Besides the two regular modes, there is a “vertical mode” which scans the bond in the perpendicular direction to the S-Au bond (Figure 7e). This is a special mode by the ELFnet and human do not read ELF images in such a way. The ELFnet scans the upper half of the ELF image such that the transition between the sulfur and gold atoms can be captured. Finally, the way the ELFnet scans the images may related to the assumption we applied to the dataset: we always place the S atom and Au atom at the left and right midpoint positions. Such assumption makes the concentration in the corner regions significant.

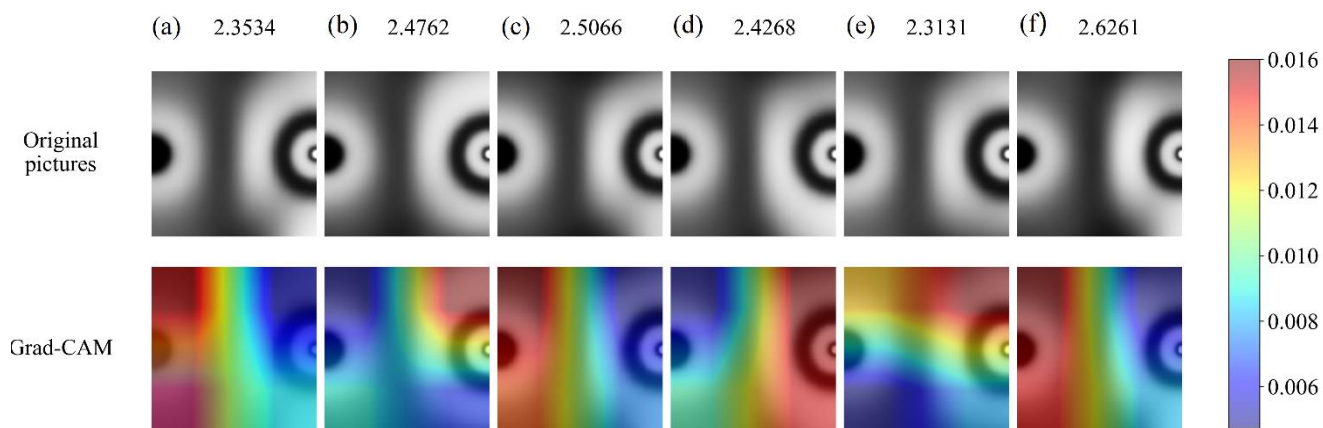


Figure 7 Grad-CAM plots of several typical patterns recognized by the ELFnet.

Besides, to further evaluate robustness of ELFnet, ELF images with occluded are used to challenge the ELFnet. In this test, each ELF image is divided into 9 zones, an ELF image with a mask can be obtained by setting values in one of 9 zones zero (Figure 8a). With such masks, the percentile degradations in MAE are summarized in Figure 8b. As expected, upper right and upper left regions are most robust to the mask. Missing information in these regions cannot fool the ELFnet much since the majority part of S-Au bond remains. In contrast, when the central region is blocked, the performance is degraded by more than 400%. Blocking the central zone makes predicting the distance between atoms really difficult. Therefore, the upper center, center and lower center regions are crucial regardless to the modes of scan explained in Figure 7.

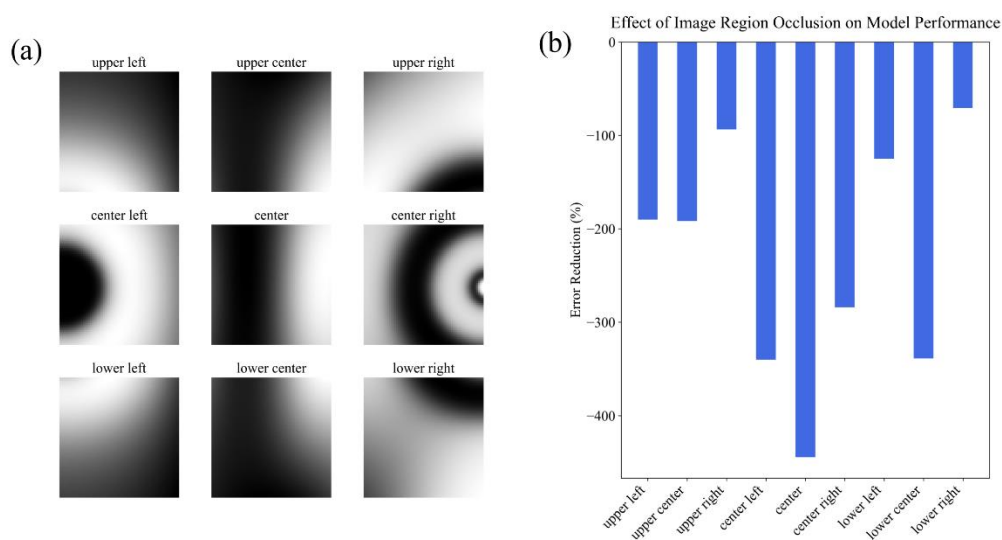


Figure 8 blocking experiments to test where are the most important regions in ELFnet recognition.

d. Application: using the ELFnet as an ELF-ruler

Before the application of the ELFnet, the concept of chemical bond should be extended based on the ELF representation. As discussed through this work, the S-Au bond types can be precisely generalized as “S-Au-2.351Å-bond”, “S-Au-2.352Å-bond”, “S-Au-2.353Å-bond” and etc. Based on the training data, all the bonds in their “natural lengths” (without extra interactions with the environment) can be recognized with a small error. Thus, the recognized bond type matches the actual bond length. However, when the molecule is distorted with other factors such as interaction with extra atoms or excited by external fields, the recognized bond type differs from the bond length. The generalized bond type provide details in the distortion of the bond length.

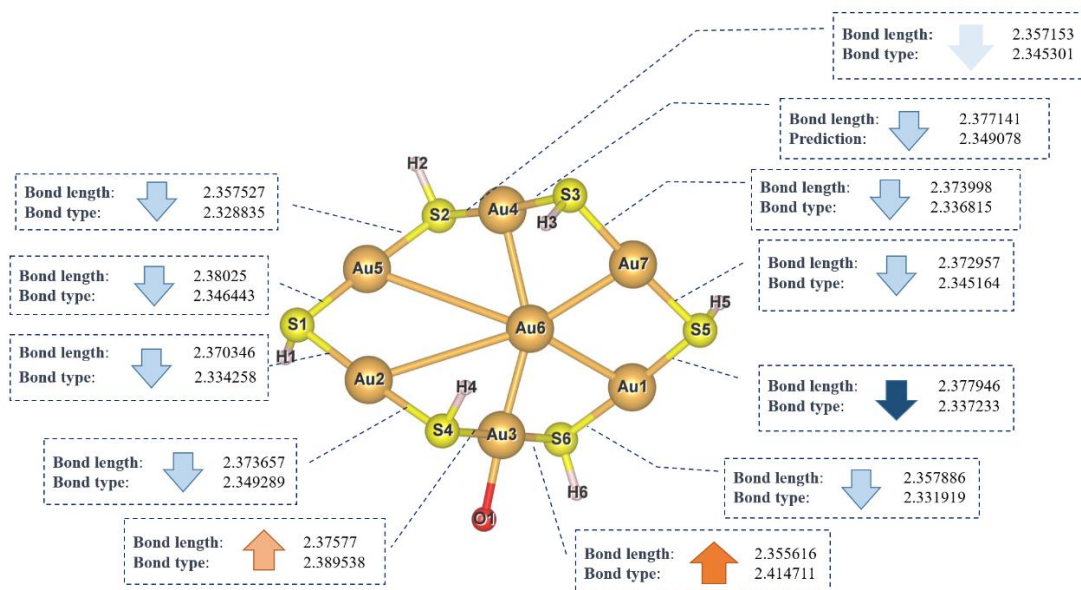


Figure 9 Applications of the ELF-ruler for S-Au bonds evaluations. a) the optimized geometry of the oxygen atom attached $Au_7(SH)_6$. Bond changes are marked.

The ELFnet is then applied to an intermediate chemical state of adhesion of an oxygen atom on a gold cluster. Such structure of adhesion can be commonly seen in many catalytic processes. The activation site is usually located on a gold atom which is noted as “Au3” in the simulation. But the “Au3” contained S-Au bonds are weakened since the predicted bond types are larger than bond lengths (Figure 9). Besides, when we focus on the ring of sulfur and gold, the two S-Au bonds near the attached oxygen atom are reduced, but most ones further away are tightened (predicted bond types are smaller than the bond lengths except S2-Au4). The adhesion of the oxygen atom causes a “ripple” pattern on the ring of gold and sulfur atoms. The weakening in bonds S4-Au3 and S6-Au3 matches people’s expectations. But the tightens of other S-Au bonds may indicate the chance in adhesion of a second oxygen atom elsewhere is small.

IV. Summary

In summary, based on the ELF image dataset which is generated by DFT simulation of TP-AuNCs in the literature, a CNN based model (the ELFnet) is trained and tested. The ELFnet with high-precision in prediction makes it suitable for the usage as a high precision “ELF-ruler” for various S-Au bonds in different physical or chemical environments. Application of oxygen adhesion in typical catalytic processes is also analyzed by the ELF-ruler where the distortion of the electron structure with a pattern extends beyond the activation site.

To build such ELFnet, the parameter space is too large to perform an exhaustive tuning. Instead, the network depth, regularization algorithms (BatchNorm and Dropout with various dropout rates), training parameters (learning rates and batch sizes) and activation/pooling algorithms (ReLU, LeakyReLU, max pooling and average pooling) are tested to find an optimal structure of the ELFnet. The optimized model, the ELFnet gives an MAE as low as 0.0021 Å after five-fold cross-validation. In addition, visualizations and interpretability analyses of ELFnet are evaluated, including an analysis of the output images from each convolutional layer, an interpretability analysis using Grad-CAM on the last convolutional layer, and an occlusion experiment. These experimental results fully demonstrate the feature extraction process of ELFnet for S-Au bonds in ELF images and the decision-making process for bond length prediction, highlighting the reliability of ELFnet in bond length prediction.

In this work, the ELFnet shows its great potential to aid human in the explanation of ELF results. Considering the versatility of the TP-AuNCs, further construction of the dataset must involve more clusters. In the synthesis process, TP-AuNCs are adjustable in their size, shape, constitution and ligands, more types of bonds such as P-Au bonds, Au-Ag bonds, S-Ag bonds and etc. should be considered. It is important to extend the ELFnet to different network architectures including networks with deeper depths, Recurrent Neural Network (RNN) and more. Such improve of ELF recognition

models will bring the chemical bond analysis for TP-AuNCs to the next level with more intuitive design and interpretation of the more adaptive cluster adjustment.

Appendix

The gold NCs collected from the literature

TP-AuNCs	Number of Au-S bond	Number of ELF's	ref
Au ₇ (SH) ₆	12	84	26
Au ₈ (SH) ₆	12	84	26
Au ₈ (SH) ₇	14	98	26
Au ₉ (SH) ₅	10	70	26
Au ₉ (SH) ₆	12	84	26
Au ₉ (SH) ₇	14	98	26
Au ₁₀ (SH) ₇	14	98	26
Au ₁₁ (SH) ₆	12	84	26
Au ₁₁ (SH) ₇	14	98	26
Au ₁₁ (SH) ₈	16	112	26
Au ₁₂ (SC ₇ H ₅ O ₂) ₆	12	84	26
Au ₁₃ (SH ₂) ₁₂	8	56	*
Au ₁₈ (SH) ₁₄	28	196	27
3-Au ₂₀ (SCH ₃) ₁₆	32	224	28
4-Au ₂₀ (SCH ₃) ₁₆	32	224	28
1-Au ₂₁ (SCH ₃) ₁₄	28	196	29
Au ₂₂ (SCH ₃) ₁₈	36	252	30
2-Au ₂₄ (SCH ₃) ₂₀	40	280	31
3-Au ₂₄ (SCH ₃) ₂₀	40	280	31
Au ₂₇ (SH) ₂₀ ⁻	40	280	32
Au ₂₈ (SCH ₃) ₂₀	40	280	33
Au ₃₂ SH ₂₁ ⁻	42	294	32
Au ₃₆ SH ₂₅ ⁻	50	350	32
Au ₃₈ (SCH ₃) ₂₄	48	229	34
Au ₄₄ (SCH ₃) ₂₈	56	392	35
Total	662	4527	

*Tabel S 1 list of collected gold nanoclusters with number of S-Au bonds and number of ELF images. References are added in the last column. * Au₁₃(SH₂)₁₂ cluster is a simplified cluster with a well-known Au₁₃ core. Though it is not a real structure from experiment, but can be used in simulations.*

The number of S-Au bonds within the key length range, along with their corresponding weights and the weighted S-Au bond count, are shown in the following table.

Range of bond length	Count	Weight	Count with duplication
[2.3 Å, 2.4 Å)	2643	1	2643
[2.4 Å, 2.5 Å)	1169	2	2338
[2.5 Å, 2.6 Å)	133	20	2660
[2.6 Å, 2.7 Å]	14	30	420
Total			8061

Tabel S 2 constitution of the training dataset. Weights are added by taking the frequency distribution over bond length as the reference.

Some ELF color plots are shown below.

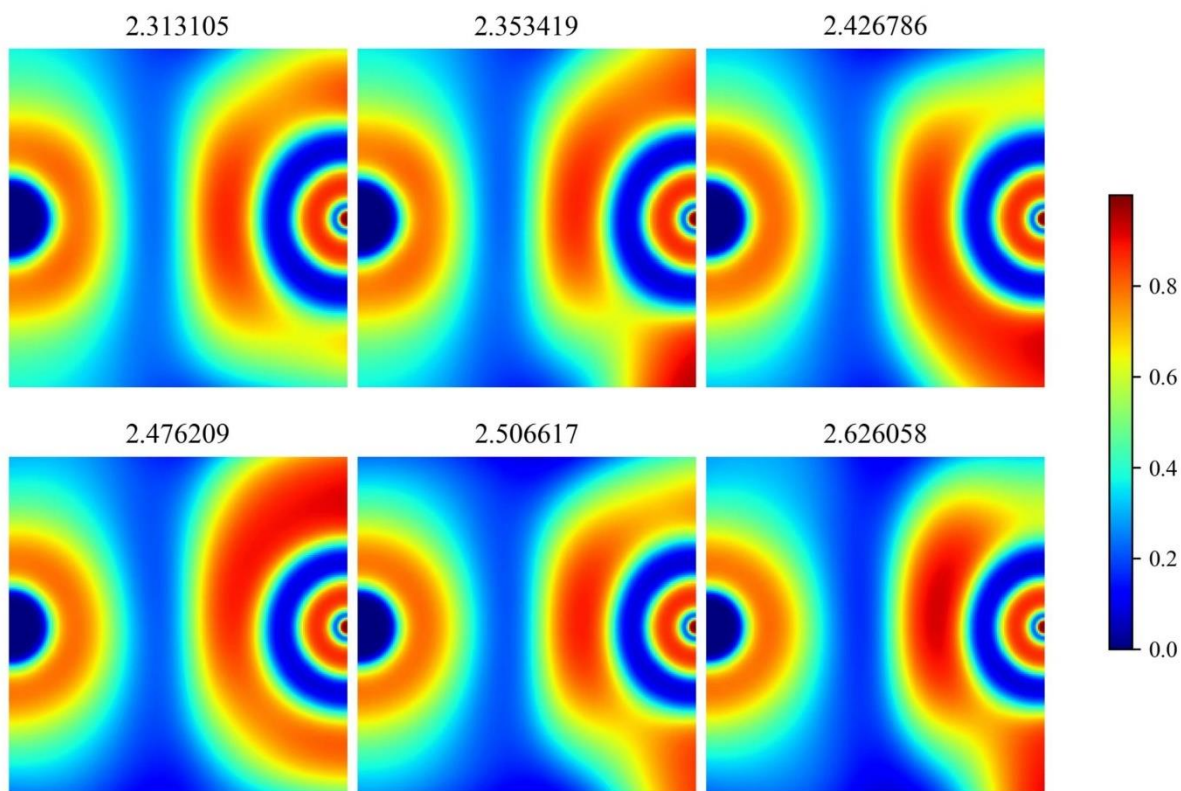


Figure S 1 ELF: selected ELF images with tags marked.

Acknowledgement

This work was supported by the National Key R&D Program of China (2021YFF1200700) and the Natural Science Foundation of China (No. 11675120 and 11535008).

Reference

1. Becke, A. D. & Edgecombe, K. E. A simple measure of electron localization in atomic and molecular systems. *The Journal of Chemical Physics* **92**, 5397–5403 (1990).
2. Savin, A. *et al.* A new look at electron localization. *Angewandte Chemie International Edition in English* **30**, 409–412 (1991).
3. Silvi, B. & Savin, A. Classification of chemical bonds based on topological analysis of electron localization functions. *Nature* **371**, 683–686 (1994).
4. Burnus, T., Marques, M. A. L. & Gross, E. K. U. Time-dependent electron localization function. *Phys. Rev. A* **71**, 010501 (2005).
5. Ullrich, C. A. *Time-dependent density-functional theory: concepts and applications*. (Oxford University Press, 2016).

6. Hao, F., Armiento, R. & Mattsson, A. E. Using the electron localization function to correct for confinement physics in semi-local density functional theory. *The Journal of Chemical Physics* **140**, 18A536 (2014).
7. Mu, X. *et al.* Redox Trimetallic Nanozyme with Neutral Environment Preference for Brain Injury. *ACS Nano* **13**, 1870–1884 (2019).
8. Vibrational Spectral Studies, Quantum Mechanical Properties, and Biological Activity Prediction and Inclusion Molecular Self-Assembly Formation of N-N'-Dimethylethylene Urea. *Biointerface Res Appl Chem* **12**, 3996–4017 (2021).
9. Abu Ali, O. A. *et al.* Synthesis, structural features, excited state properties, fluorescence spectra, and quantum chemical modeling of (E)-2-hydroxy-5-(((4-sulfamoylphenyl)imino) methyl)benzoic acid. *Journal of Molecular Liquids* **360**, 119557 (2022).
10. Fatima, A. *et al.* Quantum computational, spectroscopic, Hirshfeld surface, electronic state and molecular docking studies on sulfanilic acid: An anti-bacterial drug. *Journal of Molecular Liquids* **346**, 117150 (2022).
11. Guo, Q. *et al.* Stitching electron localized heptazine units with “carbon patches” to regulate exciton dissociation behavior of carbon nitride for photocatalytic elimination of petroleum hydrocarbons. *Chemical Engineering Journal* **452**, 139092 (2023).
12. Jin, R., Li, G., Sharma, S., Li, Y. & Du, X. Toward Active-Site Tailoring in Heterogeneous Catalysis by Atomically Precise Metal Nanoclusters with Crystallographic Structures. *Chem. Rev.* **121**, 567–648 (2021).
13. Jadzinsky, P. D., Calero, G., Ackerson, C. J., Bushnell, D. A. & Kornberg, R. D. Structure of a thiol monolayer-protected gold nanoparticle at 1.1 Å resolution. *Science (New York, N.Y.)* **318**, 430–433 (2007).
14. Heaven, M. W., Dass, A., White, P. S., Holt, K. M. & Murray, R. W. Crystal structure of the gold nanoparticle [N(C₈H₁₇)₄][Au₂₅(SCH₂CH₂Ph)₁₈]. *Journal of the American Chemical Society* **130**, 3754–3755 (2008).
15. Yamazoe, S. *et al.* Hierarchy of bond stiffnesses within icosahedral-based gold clusters protected by thiolates. *Nat Commun* **7**, 10414 (2016).
16. Taylor, M. G. & Mpourmpakis, G. Thermodynamic stability of ligand-protected metal nanoclusters. *Nat Commun* **8**, 15988 (2017).
17. Jia, H., Liu, C. & Li, Y. Doping Effects in the Thiolate-Protected Gold Nanoclusters from the Perspective of Balance Between Ligands and the Core. *J. Comput. Biophys. Chem.* **21**, 759–768 (2022).

18. Pakiari, A. H. & Jamshidi, Z. Nature and Strength of M–S Bonds (M = Au, Ag, and Cu) in Binary Alloy Gold Clusters. *J. Phys. Chem. A* **114**, 9212–9221 (2010).
19. Malola, S. *et al.* A method for structure prediction of metal-ligand interfaces of hybrid nanoparticles. *Nat Commun* **10**, 3973 (2019).
20. Pritchard, B. P., Altarawy, D., Didier, B., Gibson, T. D. & Windus, T. L. New Basis Set Exchange: An Open, Up-to-Date Resource for the Molecular Sciences Community. *J. Chem. Inf. Model.* **59**, 4814–4820 (2019).
21. Frisch, M. J. *et al.* Gaussian09. (2009).
22. Lu, T. & Chen, F. Multiwfn: A multifunctional wavefunction analyzer. *J. Comput. Chem.* **33**, 580–592 (2012).
23. Wang, X. *et al.* Dilute carbon in H3S under pressure. *npj Comput Mater* **8**, 87 (2022).
24. Wu, Y., Li, Y. & Liu, C. Uniaxial compressions induced complementarity and anisotropic behaviors in CuVP₂S₆. *J. Phys.: Condens. Matter* **35**, 135501 (2023).
25. Viennois, R., Koza, M. M., Moll, A. & Beaudhuin, M. Thermoelectric properties and lattice dynamics of tetragonal topological semimetal Ba₃Si₄. *Phys. Chem. Chem. Phys.* **25**, 1987–1997 (2023).
26. Liu, C., Pei, Y., Sun, H. & Ma, J. The Nucleation and Growth Mechanism of Thiolate-Protected Au Nanoclusters. *J. Am. Chem. Soc.* **137**, 15809–15816 (2015).
27. Senanayake, R. D. & Aikens, C. M. Theoretical investigation of relaxation dynamics in the Au₁₈(SH)₁₄ thiolate-protected gold nanocluster. *J. Chem. Phys.* **151**, 094702 (2019).
28. Jiang, D., Chen, W., Whetten, R. L. & Chen, Z. What Protects the Core When the Thiolated Au Cluster is Extremely Small? *J. Phys. Chem. C* **113**, 16983–16987 (2009).
29. Liu, C., Lin, S., Pei, Y. & Zeng, X. C. Semiring Chemistry of Au₂₅(SR)₁₈: Fragmentation Pathway and Catalytic Active site. *J. Am. Chem. Soc.* **135**, 18067–18079 (2013).
30. Pei, Y., Tang, J., Tang, X., Huang, Y. & Zeng, X. C. New Structure Model of Au₂₂(SR)₁₈: Bitetrahedron Golden Kernel Enclosed by [Au₆(SR)₆] Au(I) Complex. *J. Phys. Chem. Lett.* **6**, 1390–1395 (2015).
31. Pei, Y. *et al.* Interlocked Catenane-Like Structure Predicted in Au₂₄(SR)₂₀: Implication to Structural Evolution of Thiolated Gold Clusters from Homoleptic Gold(I) Thiolates to Core-Stacked Nanoparticles. *J. Am. Chem. Soc.* **134**, 3015–3024 (2012).
32. Lin, D., Zheng, M. & Xu, W. W. Structural predictions of thiolate-protected gold nanoclusters *via* the redistribution of Au–S “staple” motifs on known cores. *Phys. Chem. Chem. Phys.* **22**, 16624–16629 (2020).

33. Sun, X., Wang, P., Xiong, L. & Pei, Y. Theoretical prediction of a new stable structure of Au₂₈(SR)₂₀ cluster. *Chemical Physics Letters* **704**, 68–75 (2018).
34. Molina, B. *et al.* Structures and chiroptical properties of the BINAS-monosubstituted Au₃₈(SCH₃)₂₄ cluster. *Nanoscale* **5**, 10956 (2013).
35. Pei, Y., Lin, S., Su, J. & Liu, C. Structure Prediction of Au₄₄(SR)₂₈: A Chiral Superatom Cluster. *J. Am. Chem. Soc.* **135**, 19060–19063 (2013).